Nanoscale

PAPER

View Article Online
View Journal | View Issue

Cite this: *Nanoscale*, 2025, **17**, 26820

Strain-induced wave energy harvesting using atomically thin chromiteen

Royston Mathias,[a] Subhendu Mishra,[b] Abhishek Kumar Singh [b] and Partha Kumbhakar *[a]

Received 9th October 2025,
Accepted 26th October 2025

DOI: 10.1039/d5nr04273a

rsc.li/nanoscale

Developing non-corrosive wave energy harvesters is one of the critical technologies required for sustainable energy harvesting. This work studies the effect of surface defects in atomically thin chromiteen for harvesting energy from water waves. An external strain further enhances the surface charge properties of the chromiteen, resulting in higher electrical output in the fabricated flexible nanogenerator (C-FNG) to harvest wave energy. The peak output voltage of the C-FNG device was ~5 V due to the water wave force. The density functional theory (DFT) results indicate the presence of surface defects in the 2D chromiteen, and the applied strain gradient introduced a redistribution of electron density, possibly due to altered bond lengths in the material. The present work provides an atomistic study of energy harvesting in the marine environment to provide power for deep-sea divers, ships, and any other small electronic sensors or marine Internet of Things in remote areas.

Introduction

Energy sources such as solar energy, wind energy, water wave energy, and hydroelectric energy are gaining importance currently due to their low carbon footprint and sustainable energy generation.[1,2] These natural sources of power provide benefits including reduced environmental pollution, cost-effectiveness, and low maintenance, which provide a wide range of applications.[3,4] These sustainable energies can be used for small- and large-scale power generation to provide clean, affordable, and off-grid power that meets the global energy needs.[5,6] Water wave energy harvesting is one of the fast-emerging sustainable sources of energy.[7] The massive mechanical force that the sea exerts through its waves on the coastal areas is often ignored. Hence, using water wave power as the driving energy offers a sustainable way to generate electricity, which is also known as blue energy harvesting.[8–13] There are currently several types of water wave systems that are in use, but they face various challenges in providing energy to ships or offshore platforms. These systems are often made of a metal body and mechanical parts such as gears, bearings, clamps, and so on.[14] These metal parts react with the saline ocean water, causing electrochemical reactions that cause corrosion in the systems.[15] Furthermore, the large force exerted by the ocean waves causes the mechanical parts to undergo wear and tear easily. This reduces the lifetime of existing devices immensely.[16] Therefore, systems are required whose lifetime is not mostly dependent on the marine environment and do not degrade due to it. Besides this, the devices can be used to store and provide power to any other small electronic sensors or electronic devices in remote coastal areas for marine applications.

2D material-based flexible nanogenerators (2D-FNGs), such as triboelectric, flexoelectric, and piezoelectric-based nanogenerators, can be useful in this direction.[17–20] Although, triboelectric and piezoelectric nanogenerators are vastly studied for energy harvesting technology, the requirement of higher external stress and frequency makes them challenging to use in ocean wave harvesting. Flexoelectricity, on the other hand, can generate charges with a very low mechanical strain gradient or mechanical response, which develops electric polarization in the material.[21] Flexoelectricity exists in principle in all dielectric materials and has been used for different applications. Despite this phenomenon existing in all dielectric materials, there is a theoretical limit to the bulk flexoelectricity that cannot be exceeded.[22] Hence, it has been widely studied in various types of low dimensional materials like soft materials, biomembranes and 2D materials, and the flexoelectric effect provides an alternative method for device applications in electricity harvesting, sensing, and actuating. Small strains on nanoscale materials such as nanotubes, nanowires, and two-dimensional (2D) materials would give rise to large strain gradients. Moreover, 2D materials can also endure large out-of-plane deformation due to their high mechanical strength and become polarized due to a strain gradient generated by an

[a]*Department of Physics and Electronics, Christ University, Bangalore 560029, India. E-mail: partha.kumbhakar@christuniversity.in*
[b]*Materials Research Centre, Indian Institute of Science, Bangalore 560012, India*

applied external stress to generate charges.[23] Furthermore, these atomically thin materials have a higher surface area and surface charge, due to which a higher value of electric power is produced, which increases the efficiency of the FNGs.[24] These materials have one or two atomically thin layers,[25–27] due to which there is quantum confinement of electrons or holes in one dimension, and this causes the 2D materials to possess unique electronic properties and responses to external strain.[28,29] In atomically thin materials, the strain generated in them is easily propagated in only two dimensions, unlike in bulk materials.[30,31] This propagation of strain in two dimensions significantly modifies their lattice symmetry, which causes them to generate electrical signals.[32] However, for real-life applications, the 2D materials must be integrated with a matrix material, such as polymers, for increasing their durability and mechanical strength. In such 2D material-integrated polymers, the strain is applied to the polymer, and it gets propagated from the polymer matrix to the 2D materials. Hence, the technique used to integrate 2D materials into a polymer matrix is important to avoid slippage. Therefore, 2D materials are encapsulated in the polymer matrix for efficient propagation of the applied strain by water waves.[33]

In this work, we have designed a flexible energy harvesting device using the atomically thin chromiteen[34] and the thermoplastic polyurethane (TPU) polymer matrix, which generates charges based on the flexoelectric principles. The 2D chromiteen provided high surface charge for efficient charge generation, and the TPU polymer provided flexibility to sustain in the harsh marine environment and an effective strain propagation property to chromiteen. The fabricated device was tested for its output voltage by means of an indigenously designed ocean simulator. By varying various physical parameters like the depth of the film in water, the frequency of waves, and the aspect ratio of the film, the output efficiency was optimised. Density functional theory calculations were further used to get more insight into the efficiency. Therefore, the fabricated C-FNG can be used as a portable power source for ships, for emergency situations, and as a backup. Moreover, it can provide power supply for fishermen in places with limited resources to enhance their efficiency and safety.

Experimental section

Materials

The chromite ore ($FeCr_2O_4$) was supplied by a mine in Orissa, India. 99.8% pure TPU polymer and dimethylformamide (DMF), 99.5% pure acetone and 4 mT magnetic field super magnets were supplied by Sigma-Aldrich, Bangalore, India.

The synthesis of a few atomic-layer thin chromiteen

The bulk chromite ore was first crushed using a grinder to make the particles finer. The crushed chromite ore particles were then added to DMF solvent to prepare a dispersed solution. The ratio of chromite to DMF was 1 mg : 5 ml, which was an optimum amount for a well-dispersed solution. The solution was then subjected to exfoliation using the Liquid Phase Exfoliation (LPE) technique. The solution was sonicated for 5 hours in a probe sonicator at room temperature. The probe sonication was carried out with a 10 s ON pulse and a 5 s OFF pulse to avoid overheating of the sample. Moreover, the solution was kept in an ice bath to maintain room temperature. The LPE method was used due to its scalability and ability to exfoliate the bulk material into atomically thin 2D sheets. The bulk chromite ore has a layered structure, and during exfoliation, nanobubbles are formed due to the ultrasonic waves in the solution. These nanobubbles enter the layers of the chromite ore and burst. This burst releases a large amount of energy, which breaks the van der Waals bonds that hold the layers together. Finally, the layers get separated, and the exfoliated chromite sample is obtained. Furthermore, the exfoliated sample is left to rest for 24 hours after the exfoliation process. This ensures that the bulk particles settle down and only the exfoliated chromite, which is at the top part of the solution, is separated for further use.

Fabrication of the C-FNG device

The fabrication of the C-FNG device started by dissolving the TPU polymer in DMF solvent. 4.7 g of TPU was dissolved in 20 ml of DMF. Furthermore, the exfoliated chromite sample was added to the dissolved TPU. This mixture was thoroughly mixed for 5 minutes to achieve a uniform distribution of chromite particles in the TPU. Furthermore, the mixture was poured into a Petri dish, which was placed on permanent magnets. These magnets produced a magnetic field that aligned the chromite particles in the TPU in the same direction. This ensured that the charge generation process was not affected by the randomness in the 2D chromite particle orientation. The poured solution was left as it is for 24 hours to dry and cure. The DMF solvent was vaporised during this process, and only the TPU–chromite composite was left behind, which was in the form of a polymer film.

Furthermore, to fabricate the C-FNG device, the film was attached with two copper electrodes that were connected on either side of the film to allow the electrons to flow through them (Fig. S1). Furthermore, the electrical characteristics such as output voltage, output current, internal resistance, and power output of the device were measured.

Strain generation in the chromiteen–TPU composite film

The synthesized C-FNG film was subjected to a uniaxial strain applied to both extremes of the film. This caused the film to bend, and the strain was propagated to the 2D chromiteen sheets in the composite. The strain (ε) in the film was calculated using the equation,[35]

$$\varepsilon = \frac{\tau}{R} \quad (1)$$

where τ is half the thickness of the film and R is the radius of curvature of the bent composite film. The film was bent to five different strain values of 0%, ~1.6%, 2.05%, 2.6%, and 4.2%.

Characterization

The 2D sheet structure and the morphology of the exfoliated sample can be seen using a Scanning Electron Microscope (SEM) from ThermoFisher (Apreo S LoVac), which was attached to an energy dispersive spectrometer (EDS) to confirm the relative composition of the sample. X-ray diffraction (Miniflex 600 Rigaku XRD) was carried out to confirm the different phases and Miller indices of planes exposed during the exfoliation. High-Resolution Transmission Electron Microscopy (HRTEM) (Talos F200 G2) was used to analyse the defects in the atomic structure of the sample. Raman spectroscopy (Renishaw inVia Raman Microscope) was carried out to understand the modifications in the lattice structure of the chromiteen under strain. Fourier Transform Infrared Spectroscopy (FTIR) was used to gain further insights into the bonding between the 2D chromite and TPU polymer and the chemical properties of the C-FNG film. The tensile strength of the C-FNG was measured using a Universal Tensile Testing Machine (UTTM) from Finetechno Engineering. The film used for testing measured 17 mm × 10 mm × 0.3 mm ($l \times b \times h$). The film was clamped onto the UTTM machine, where it was elongated until it reached its breakdown point. The film was stretched out at a rate of 5 mm per minute.

First-principles calculations

We carried out first-principles density functional theory (DFT) calculations using the Vienna *Ab Initio* Simulation Package (VASP).[36,37] The interactions between ions and electrons were modeled using projector-augmented wave (PAW) potentials,[38,39] and the exchange–correlation effects were treated within the Perdew–Burke–Ernzerhof (PBE) formulation of the generalized gradient approximation (GGA).[40] A plane-wave basis set with an energy cutoff of 500 eV was used to represent the Kohn–Sham orbitals. For structural optimization, the conjugate-gradient algorithm was employed until the Hellmann–Feynman forces on each atom were reduced below 0.005 eV $Å^{-1}$. The Brillouin zone was sampled using a Γ-centered Monkhorst–Pack (MP) k-point mesh of 8 × 8 × 8, ensuring convergence during geometry optimization. To investigate the charge transfer between Fe/Cr and O atoms in $FeCr_2O_4$, the Bader charge analysis was employed.[41,42] In this method, the net atomic charge was calculated using the formula: Bader net atomic charge = ZVAL − Bader population. Here, ZVAL denotes the number of valence electrons associated with each atomic species. Additionally, the charge density difference can be computed to visualize the redistribution of electrons. This is typically defined as[43,44] $\Delta\rho(r) = \rho FeCr_2O_4(r) - \rho CrFe(r) - \rho O(r)$, where, $\rho FeCr_2O_4(r)$, $\rho CrFe(r)$, and $\rho O(r)$ are the charge densities of $FeCr_2O_4$, CrFe and O, respectively.

Results and discussion

Structural and morphological properties of the C-FNG film

The XRD spectra of the exfoliated sample were recorded to study the crystallinity of the material. It was observed that the XRD pattern of the exfoliated sample matched the spinel phase of chromite [JCPDS No.: mp-1104680] (Fig. S2). The Miller indices (h,k,l) of the planes were also determined using the XRD data. AFM characterisation was carried out to study the sheet thickness of the exfoliated and synthesized chromiteen (Fig. 1a and b). Fig. 1a shows the gradual decrease in the thickness of the synthesized chromiteen with increasing exfoliation time. Few atomic layer thick chromiteen was obtained after 5 hours of exfoliation (Fig. 1b). The inset of Fig. 1b shows the profile plot of the surface of a single sheet obtained from the LPE method, which was found to be 6 nm. This confirms the formation of a few atomically thin sheets of chromiteen. Fig. S3 shows the AFM images of the gradual formation of chromiteen sheets from the chromite ore over a period of 4 hours of exfoliation. The TEM images of the chromite sample were also obtained to confirm the layered nature of the exfoliated sample, as shown in Fig. 1c. In Fig. 1c, we also marked the presence of a few layers of chromiteen. The HRTEM image of the 2D layered chromite sample was obtained to check the presence of lattice defects (Fig. 1d). The fast Fourier transformation (FFT) pattern of the HRTEM image showed irregularity in the atomic positions in the sample, implying the presence of defects in it (Fig. 1e). Furthermore, the atomic arrangement (marked in yellow squares in Fig. 1d)

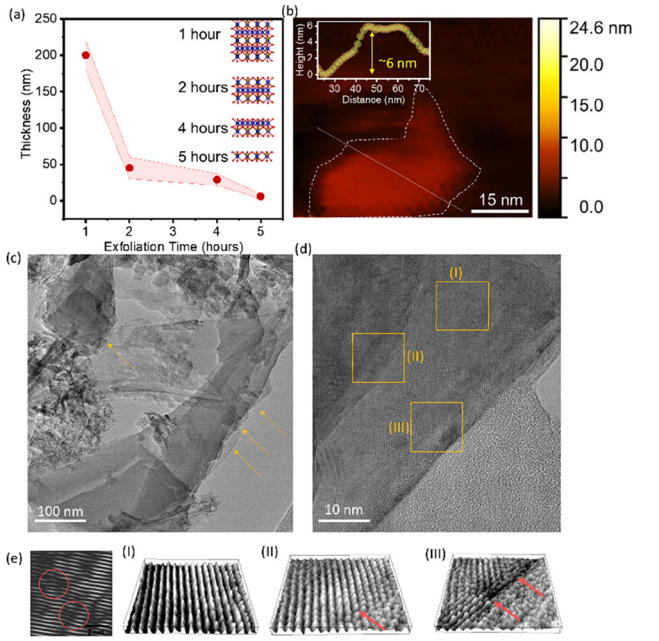

Fig. 1 (a) Plot showing the change in layer thickness of the chromite ore with increasing exfoliation time. The inset shows the schematic of reducing thickness of chromiteen. (b) AFM image of the 5-hour exfoliated chromiteen. The inset shows the profile plot of the AFM image. (c) TEM image of the exfoliated chromiteen, confirming the 2D sheet structure. (d) HRTEM image of the chromiteen showing the atomic arrangement in the sample. (e) FFT pattern of the HRETM image showing the irregularities in the atomic arrangement. ((e) I–III) 3D plots of the HRTEM image of the positions marked with yellow squares in (d), visualizing the defects and irregularities in the atomic arrangement.

from the HRTEM image was 3D plotted (Fig. 1eI–III) using ImageJ software to visualize the atomic positions and the defects present in it. Fig. 1eII–III show the defects in the atomic arrangement which is generated during the liquid phase exfoliation process of the chromite ore. The presence of surface defects in chromiteen can be a source of charge generation under strain conditions. Furthermore, characterization studies were carried out to understand the molecular bonding in the atomically thin chromiteen sample and its interaction with the polymer using FTIR measurements. Fig. S4a shows the FTIR spectra of the synthesized sample, which were recorded over the wavelength range of 500–4000 cm^{-1}, confirming the spinel phase of chromiteen. We have also measured the zeta potential to study the surface of the materials, and it was found to be −32.4 mV, which implies the presence of a net negative charge on the surface of the material (Fig. S4b).

Voltage generation in C-FNG under strain conditions

As shown in Fig. 2a, C-FNG was subjected to uniaxial strain by bending it mechanically. As discussed in the synthesis process, the chromiteen is encapsulated within the polymer matrix, and hence, there is no slippage between them during the straining process, as shown in the schematic diagram in the inset of Fig. 2b. By avoiding this slippage, the strain is transferred from the polymer to the 2D sheets efficiently. Furthermore, strain was applied to both ends of the flexible film to observe the changes in the surface charge of chromiteen by observing the generated output voltage. As shown in Fig. S5, the output voltage of the unstrained flexible composite film was ~2.72 ± 0.08 V (V_{pp}). However, when a strain was applied, the output voltage increased and reached a value of ~3.76 ± 0.08 V (V_{pp}) at an applied strain of ~4.2% (Fig. 2b). This indicated that the strain in the device was efficiently transferred to the chromiteen structure. The strain gradient causes a change in the lattice symmetry of the chromiteen and thereby a change in the surface charge (Fig. 2c). Hence, the charge generation in the device occurs due to the flexoelectricity principle. As explained using DFT in the later section, when strain is applied, a redistribution of electron density occurs due to altered bond lengths or angles. These changes in bond lengths and redistribution of electron density generate electric polarisation in the material, which causes chromiteen to generate charges. These charges flow out of the device through the metal electrodes connected to the C-FNG device. This process continues for both the to and fro motion of the film in the water wave and generates voltage for both cycles due to the strain generated in it.

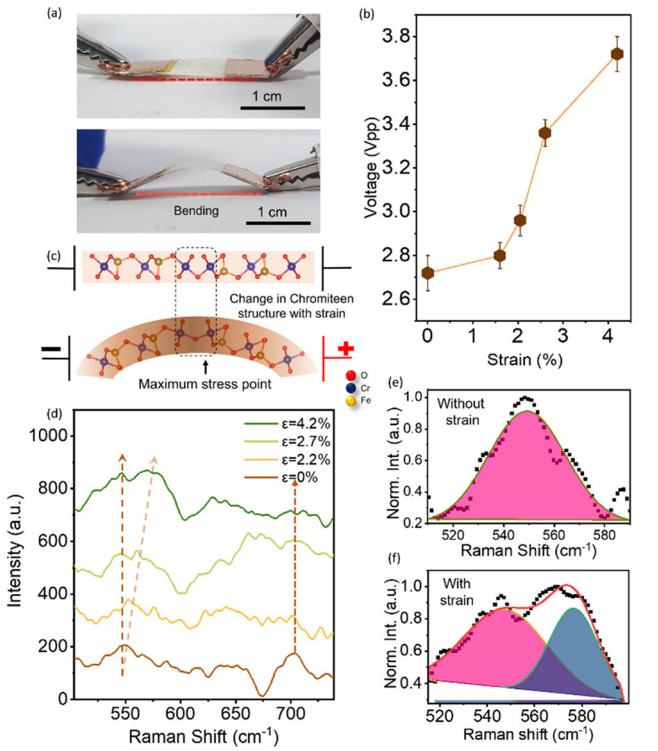

Fig. 2 (a) Digital images of the uniaxial strain applied to the C-FNG device. (b) Plot showing the change in the output voltage of the C-FNG device with the change in strain. (c) Schematic diagram showing the flexoelectricity mechanism for chromiteen bending due to strain propagation from the TPU matrix. (d) Change in the peak position of the Raman spectrum due to the applied strain in the C-FNG device. (e) Magnified Raman peak of the unstrained chromiteen. (f) The peak splitting in the Raman spectrum due to the broken lattice symmetry in chromiteen.

This phenomenon was confirmed using *in situ* Raman spectroscopy on the unstrained and strained C-FNG. As shown in Fig. 2d, the unstrained film (ε = 0%) showed two prominent Raman peaks at wavelengths of 549 cm^{-1}, which corresponds to F_{2g} symmetry, and 703 cm^{-1}, which corresponds to A_{1g} symmetry, which are characteristic Raman peaks for chromiteen 2D sheets. Furthermore, the flexible film was subjected to gradual strain of 2.2%, 2.7%, and 4.8% under a Raman system, which showed a shift in the characteristic peak positions. Fig. 2e shows a peak at 549 cm^{-1} with F_{2g} symmetry for the unstrained film. This peak gradually split into two peaks at wavelengths of 546 cm^{-1} and 570 cm^{-1} at a maximum strain of 4.2% (Fig. 2f). This indicates that the strain is effectively transferred from the polymer matrix to the chromiteen sheets, and its lattice symmetry is broken at this strain level.

First-principles calculations

To study the effects of surface defects and strain on charge generation, we conducted DFT calculations in detail. The crystal structure of $FeCr_2O_4$ is shown in Fig. 3a, with optimized lattice parameters a = 10.05, b = 6.055, and c = 5.93 Å. The corresponding density of states (DOS) is shown in Fig. 3b. The upper and lower panels represent spin-up and -down states, respectively. The non-uniform distribution of spin-up and spin-down states results in non-zero magnetization with a magnetic moment of ~6.06μ_B. The total DOS shows a continuous distribution of states across the Fermi level, confirming that electrons can occupy energy levels without any forbidden region. The partial DOS reveals that the Cr d and Fe d orbitals contribute significantly near the Fermi level, with O(p) orbitals

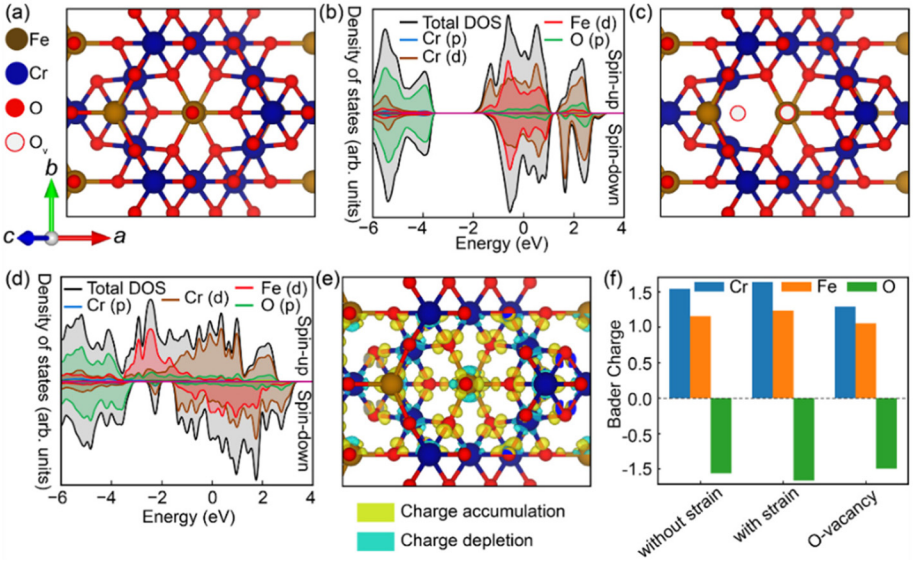

Fig. 3 A comprehensive analysis of the structural, electronic, and charge characteristics of $FeCr_2O_4$ under different conditions. (a) The crystal structure of $FeCr_2O_4$ and (b) the density of states (DOS) for the pristine case. (c) The crystal structure of $FeCr_2O_4$ with an oxygen vacancy (O_v) and (d) the corresponding density of states (DOS). (e) Charge density difference plot for the pristine structure, highlighting charge accumulation around oxygen atoms and depletion near Fe and Cr atoms. (f) Bader charge analysis under three conditions: pristine, strained, and oxygen-deficient $FeCr_2O_4$.

dominating the lower energy range (valence region). This suggests strong hybridization between transition metal d-states and oxygen p-states.

Fig. 3c shows the crystal structure of $FeCr_2O_4$ with an oxygen vacancy (O_v), marked by a circle with a white center. The optimized lattice parameters are a = 10.00, b = 5.65, and c = 5.69 Å. In contrast to the pristine case, the oxygen-deficient structure (Fig. 3d) shows a noticeable enhancement of the DOS near the Fermi level, particularly from Fe d and Cr d orbitals. The O(p) contribution is slightly reduced, reflecting the loss of oxygen coordination. This redistribution of states indicates that the vacancy introduces localized electronic states and increases the carrier density, potentially enhancing conductivity and modifying magnetic interactions. The asymmetry between spin-up and the spin-down channels also becomes more pronounced compared to the pristine case, which results in a magnetic moment of ~20.06μ_B. This comparison underscores how oxygen vacancies can be used to tune the electronic and magnetic properties of $FeCr_2O_4$, making it a versatile material for functional applications. Fig. 3e presents the charge density difference plot for pristine $FeCr_2O_4$, offering a spatial visualization of how electronic charge is distributed within the crystal structure. In this plot, yellow regions represent charge accumulation, while cyan regions indicate charge depletion. In the pristine structure, the charge accumulation is primarily observed around the oxygen atoms (red spheres). Correspondingly, the cyan regions near Fe and Cr atoms indicate that these atoms donate electron density. The plot thus confirms the partially covalent nature of bonding in $FeCr_2O_4$, where transition metal cations not only partially transfer charge to oxygen anions but also engage in some degree of covalent hybridization, especially through d–p orbital overlap. Fig. 3f presents a Bader charge analysis for $FeCr_2O_4$ under three distinct conditions: without strain, with strain, and with an oxygen vacancy. In the pristine (unstrained) case, Cr atoms carry a relatively high positive charge (~1.52e^-), Fe atoms have a moderate positive charge (~1.1e^-), and O atoms exhibit a negative charge (~1.52e^-). When strain (~1%) is applied, the charges in both Cr and Fe become more positive, while the charge in oxygen becomes more negative, indicating a redistribution of electron density, possibly due to altered bond lengths or angles (charge transfer from Cr/Fe to O atoms). The anomalous changes occur with the introduction of an oxygen vacancy. The charges in Cr and Fe become less positive, implying reduced oxidation or weaker bonding due to the missing oxygen. Interestingly, the remaining O atoms become less negatively charged (charge transfer from O to Cr/Fe), likely due to the reduced number of oxygen sites. Furthermore, the oxygen vacancies in the chromiteen were experimentally confirmed using XPS spectra (Fig. S6a). The peak fitting of the high-resolution oxygen spectra shows 3 peaks (Fig. S6b). These extra peaks, mainly at lower energy levels, suggest the presence of oxygen vacancies in the sample.

Output performance of the device under water waves

To measure the output performance of the C-FNG device under water waves (Fig. 4a), we connected the device to a DSO. The test was conducted in an indigenously designed ocean simulator, as shown in Fig. 4b (digital image of the setup). Various parameters of the experiment were varied to simulate the sea waves. Fig. 4c shows a schematic of the array of C-FNG films to harvest energy at the seashore. During the experiment, the variation of the output voltage of the device was recorded by changing the depth of the film dipped in the water, the fre-

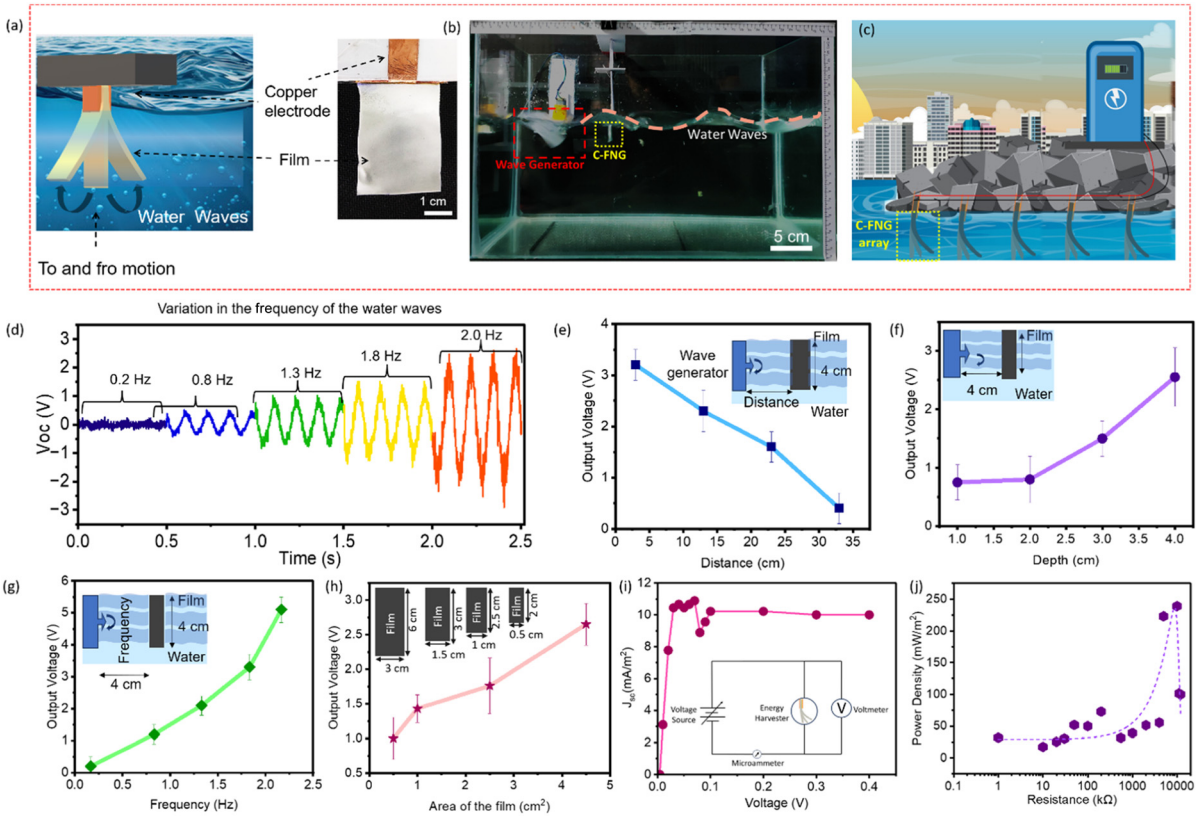

Fig. 4 (a) Schematic diagram of the C-FNG device employed underwater. The right inset shows the digital image of the C-FNG device. (b) Indigenous setup used to test the C-FNG device under various parameters. (c) Schematic diagram showing the applicability of the C-FNG devices at the seashore for wave energy harvesting. (d) Transient behaviour of the C-FNG device with varying frequencies of water waves. (e) Plot of output voltage *versus* the distance of the C-FNG from the water wave source. (f) Plot of output voltage *versus* the depth of the film in water. (g) Plot of the output voltage of C-FNG *versus* the frequency of water waves. (h) Plot of output voltage *versus* the area of the C-FNG device. (i) Current density *vs.* voltage plot of the C-FNG device. The inset shows the circuit diagram used to characterise the current–voltage behaviour of the device. (j) Power density *vs.* resistance curve of the C-FNG device.

quency of waves, the aspect ratio of the film (area of the film), and the distance of the film from the source of the waves. Fig. S7a–c and Fig. 4d show the transient behaviour of the C-FNG device under different conditions.

First, we varied the distance of the film from the source of the waves from 33 cm to 3 cm (inset of Fig. 4e). The voltage obtained when the film was at a distance of ~3 cm from the source was ~3.2 V (Fig. 4e). Therefore, when the film was closer to the source of the waves, it generated more voltage than when it was farther away. This is because the waves were more turbulent when the film was closer, and therefore the film oscillated more rapidly. This caused a higher strain in the device and it generated voltage.

Furthermore, the depth of the film was varied when the film was at a constant distance of ~4 cm from the source of waves with a wave frequency of ~2 Hz. We observed that as the depth of the film inside the water was increased, the output voltage increased. When the film was completely exposed to the sea waves (depth = 4 cm), we obtained an output voltage of ~2.6 V (Fig. 4f). This implied that the greater the area of the film exposed to the sea waves, the more voltage was generated.

Furthermore, to confirm the increase in voltage when the film was brought closer to the source of water waves, we generated more turbulent waves by increasing the frequency of the waves, and it was seen that the voltage generated also increased with the increasing frequency of the waves. A voltage of ~5.1 V was obtained when the frequency of the waves was 2 Hz (Fig. 4g). Also, to confirm the increase in voltage when the depth of the film was increased in water, we changed the area of C-FNG while keeping the depth constant to confirm that the voltage increased due to the increase in the area of the film. We observed that as the area of the film increased, the output voltage also increased. The output voltage was ~2.7 V when the area of the film was ~4.5 cm^2 (Fig. 4h). These results confirm that the fabricated C-FNG device generated voltage under different marine conditions.

The power output of the device was measured using the maximum power theorem. The device was connected across a load resistance through a diode rectifier circuit, and the voltage drop was measured across the load resistance (Fig. S8a). Furthermore, the current density of the device was measured using the circuit shown in the inset of Fig. 4i. A voltage source was used to increase the potential across the

electrodes of the C-FNG device, and the voltage drop was also measured across the device. Simultaneously, the current through the device was measured using a microammeter, as shown in the circuit diagram, and a current–voltage plot was obtained, as shown in Fig. S8b. The current density was calculated by dividing the current values by the area of the C-FNG device. Finally, the current density *versus* the voltage curve was plotted (Fig. 4i), and hence, the maximum current density delivered by the device was ~10 mA m^{-2}.

Furthermore, the power density of the device was calculated using the resistance-voltage values. It was observed that a maximum power of ~239 mW m^{-2} was transferred from the C-FNG device to the load when the load resistance value was ~10 MΩ (Fig. 4j). These electrical output values showed an enhancement in the power and current values compared to the other reported devices. Table S1 gives a detailed comparison of the electrical output values of the reported flexible nanogenerators.

Study of durability and the effect of saltwater on the C-FNG device

As the C-FNG is applied for wave energy harvesting, it has to go through large mechanical force due to the oceanic waves. Hence, to validate its mechanical strength, a tensile strength measurement of the C-FNG device was carried out. Fig. S9 shows the stress–strain curve of the C-FNG sample. The strain increased with increasing stress on the film. The elongation continued until it reached a strain percentage of ~369% of its initial length, and further stress caused the film to break at a strain percentage of ~382% of its initial length. The film could withstand a load of 3 kgF, and the tensile strength of the film at the highest strain was 1.022 kg mm^{-2}. These results imply that the C-FNG device can maintain its mechanical strength under the harsh conditions of the oceans.

The high tensile strength of the C-FNG film is due to the 2D layers of chromiteen in the TPU matrix. These 2D sheets act as nanofillers that enhance the mechanical properties of the film by interconnecting the polymer chains with each other in the TPU matrix. When the ocean waves hit the polymer film, the stress gets distributed throughout due to the presence of 2D sheets and hence avoids strain at one single point. This prevents the film from tearing or generating cracks, and therefore, it enhances the overall mechanical strength of C-FNG.

To study the durability and anti-corrosion property of the C-FNG device, it was kept in saline water at a concentration of 35 g L^{-1}, which is the natural salt concentration of seawater.[45] The C-FNG was kept dipped in the solution for 5 days, and then its tensile strength was measured. It was observed that the film elongated until it reached a strain percentage of ~269% of its initial length, and further stress caused the film to break at a strain percentage of ~316% of its initial length, which is comparable to the newly synthesized film (Fig. S9). Therefore, the synthesised film shows good mechanical stability under marine conditions. Furthermore, the output voltage of the saltwater-dipped C-FNG device was measured. It was observed that the voltage output (V_{oc}) of the device dropped by ~35% due to the saltwater reaction. As 2D materials are prone to oxidation, prolonged dipping of the C-FNG film in the saltwater oxidises the chromiteen surface. This produces a net negative surface charge due to excess oxygen atoms and hence reduces the potential difference generated in the device. Fig. S10 shows the change in the output voltage of the device before and after treating it with saltwater. Furthermore, the optical image of the device surface showed discolouration due to the saltwater. This discolouration can also be attributed to the oxidation of Fe atoms present in the chromiteen structure.

Conclusions

In summary, this study reveals the modification of surface charge by applying strain in the atomically thin chromiteen. This modification of surface charge helped in generating an electric signal from ocean waves for the harvesting of energy. Furthermore, the DFT calculations confirm the presence of surface defects and generation of surface charge by the applied strain, which together improve the output performance under mechanical impact. Additionally, the durability and the anti-corrosion behaviour of the C-FNG device also prove a significant advancement in water wave energy harvesting. The high tensile strength and the presence of surface charge in the material can generate high electrical output in the device and withstand harsh ocean environments for a long period of time, providing electricity for marine applications.

Conflicts of interest

There are no conflicts to declare.

Data availability

The data supporting this article have been included as part of the supplementary information (SI). Supplementary information is available. The supporting information contains material characterization data such as XRD pattern, exfoliation time dependent AFM images, FTIR plot, zeta potential and XPS spectra of Chromiteen. It also contains results related to the output performance of the C-FNG device such as the DSO output of the strained and unstrained C-FNG, transient behaviour of the C-FNG device with various parameters, current-voltage plot, and the corrosion behaviour of the C-FNG device in the saline water. See DOI: https://doi.org/10.1039/d5nr04273a.

Acknowledgements

R.M. and P.K. are thankful to Christ University for providing research facilities. S.M. and A.K.S. thank the Materials Research Centre (MRC), Supercomputer education and research centre (SERC) and SSCU, IISc Bangalore.

References

1 A. El-Hady, B. Kashyout, A. Hassan, G. Hassan, H. El-Banna Fath, A. El-Wahab Kassem, H. Elshimy, R. Vepa and M. H. Shaheed, *RSC Adv.*, 2021, **11**, 13201–13219.
2 K. H. H. Aziz, F. S. Mustafa, K. M. Omer, S. Hama, R. F. Hamarawf and K. O. Rahman, *RSC Adv.*, 2023, **13**, 17595–17610.
3 Q. Schiermeier, J. Tollefson, T. Scully, A. Witze and O. Morton, *Nature*, 2008, **454**, 816–823.
4 O. Krishan and S. Suhag, *Int. J. Energy Res.*, 2019, **43**, 6171–6210.
5 Y. Glemarec, *Energy Policy*, 2012, **47**, 87–93.
6 J. M. Aberilla, A. Gallego-Schmid, L. Stamford and A. Azapagic, *Appl. Energy*, 2020, **258**, 114004.
7 A. F. d. O. Falcão, *Renewable Sustainable Energy Rev.*, 2010, **14**, 899–918.
8 Y. Wang, X. Liu, Y. Wang, H. Wang, H. Wang, S. L. Zhang, T. Zhao, M. Xu and Z. L. Wang, *ACS Nano*, 2021, **15**, 15700–15709.
9 Y. Bian, T. Jiang, T. Xiao, W. Gong, X. Cao, Z. Wang and Z. L. Wang, *Adv. Mater. Technol.*, 2018, **3**, 1700317.
10 Y. Jie, X. Jia, J. Zou, Y. Chen, N. Wang, Z. L. Wang and X. Cao, *Adv. Energy Mater.*, 2018, **8**, 1703133.
11 Y. Wang, E. Yang, T. Chen, J. Wang, Z. Hu, J. Mi, X. Pan and M. Xu, *Nano Energy*, 2020, **78**, 105279.
12 A. Yang, Y. Qiu, D. Yang, K. Lin and S. Guo, *RSC Adv.*, 2021, **11**, 3363–3370.
13 J. Falnes, *Mar. Struct.*, 2007, **20**, 185–201.
14 W. Li, Y. Liu, W. Sun, H. Wang, W. Wang, J. Meng, X. Wu, C. Hu, D. Wang and Y. Liu, *J. Mater. Chem. A*, 2024, **12**, 26493–26501.
15 Y. Liu, G. Sun, Y. Liu, W. Sun and D. Wang, *Front. Mater. Sci.*, 2021, **15**, 601–610.
16 C. Xu, Y. Liu, Y. Liu, Y. Zheng, Y. Feng, B. Wang, X. Kong, X. Zhang and D. Wang, *Appl. Mater. Today*, 2020, **20**, 100645.
17 M. Xu, Y.-C. Wang, S. L. Zhang, W. Ding, J. Cheng, X. He, P. Zhang, Z. Wang, X. Pan and Z. L. Wang, *Extreme Mech. Lett.*, 2017, **15**, 122–129.
18 M. Xu, S. Wang, S. L. Zhang, W. Ding, P. T. Kien, C. Wang, Z. Li, X. Pan and Z. L. Wang, *Nano Energy*, 2019, **57**, 574–580.
19 J. Huang, J. Shao, W. Zhong, C. Sun, G. Zhang, L. Chen, J. Fang, C. Li, J. Wang, X. Feng, L. Zhou, H. Mi, J. Chen, X. Dong and X. Liu, *Small Methods*, 2024, **8**, 2400078.
20 J. An, Z. M. Wang, T. Jiang, X. Liang and Z. L. Wang, *Adv. Funct. Mater.*, 2019, **29**, 1904867.
21 B. Wang, S. Yang and P. Sharma, *Phys. Rev. B*, 2019, **100**, 35438.
22 J. Narvaez, F. Vasquez-Sancho and G. Catalan, *Nature*, 2016, **538**, 219–221.
23 F. Ahmadpoor and P. Sharma, *Nanoscale*, 2015, **7**, 16555–16570.
24 R. Mondal, R. Mathias, L. V. Bastos, C. C. Gowda, N. Tiwari, H. Singh, C. F. Woellner, C. S. Tiwary and P. Kumbhakar, *Nanoscale*, 2025, **17**, 14647–14659.
25 A. Castellanos-Gomez, N. Agraït and G. Rubio-Bollinger, *Appl. Phys. Lett.*, 2010, **96**, 213116.
26 Y.-J. Zeng, D. Wu, X.-H. Cao, W.-X. Zhou, L.-M. Tang and K.-Q. Chen, *Adv. Funct. Mater.*, 2020, **30**, 1903873.
27 M. Xu, T. Liang, M. Shi and H. Chen, *Chem. Rev.*, 2013, **113**, 3766–3798.
28 A. Pal, S. Zhang, T. Chavan, K. Agashiwala, C.-H. Yeh, W. Cao and K. Banerjee, *Adv. Mater.*, 2023, **35**, 2109894.
29 L. N. Tripathi, O. Iff, S. Betzold, Ł. Dusanowski, M. Emmerling, K. Moon, Y. J. Lee, S.-H. Kwon, S. Höfling and C. Schneider, *ACS Photonics*, 2018, **5**, 1919–1926.
30 S. Yang, Y. Chen and C. Jiang, *InfoMat*, 2021, **3**, 397–420.
31 H. J. Conley, B. Wang, J. I. Ziegler, R. F. Haglund Jr., S. T. Pantelides and K. I. Bolotin, *Nano Lett.*, 2013, **13**, 3626–3630.
32 A. Varghese, A. H. Pandey, P. Sharma, Y. Yin, N. V. Medhekar and S. Lodha, *Nano Lett.*, 2024, **24**, 8472–8480.
33 Z. Li, Y. Lv, L. Ren, J. Li, L. Kong, Y. Zeng, Q. Tao, R. Wu, H. Ma, B. Zhao, D. Wang, W. Dang, K. Chen, L. Liao, X. Duan, X. Duan and Y. Liu, *Nat. Commun.*, 2020, **11**, 1151.
34 T. P. Yadav, S. N. Shirodkar, N. Lertcumfu, S. Radhakrishnan, F. N. Sayed, K. D. Malviya, G. Costin, R. Vajtai, B. I. Yakobson, C. S. Tiwary and P. M. Ajayan, *Adv. Mater. Interfaces*, 2018, **5**, 1800549.
35 C. Shang, W. Wang, J. Zhang, Y. Zhao, J. Li, L. Chen, G. Jia, N. Zhou, G. Liu, M. Hui, H. Huang, L. Zhang, G. Dong, J. Zhang, H. Xu, X. Li and R. Yang, *Adv. Funct. Mater.*, 2024, **34**, 2410783.
36 G. Kresse and J. Furthmüller, *Phys. Rev. B: Condens. Matter Mater. Phys.*, 1996, **54**, 11169–11186.
37 G. Kresse and J. Furthmüller, *Comput. Mater. Sci.*, 1996, **6**, 15–50.
38 P. E. Blöchl, *Phys. Rev. B: Condens. Matter Mater. Phys.*, 1994, **50**, 17953–17979.
39 J. P. Perdew, K. Burke and M. Ernzerhof, *Phys. Rev. Lett.*, 1996, **77**, 3865–3868.
40 G. Kresse and D. Joubert, *Phys. Rev. B: Condens. Matter Mater. Phys.*, 1999, **59**, 1758–1775.
41 P. Kumbhakar, S. Mishra, P. Kumbhakar, R. K. Barik, C. S. Tiwary and A. K. Singh, *J. Phys. Chem. C*, 2024, **128**, 10733–10741.
42 P. Kumbhakar, S. Mishra, C. C. Gowda, P. M. Nishma, A. Venugopal, A. K. Singh and C. S. Tiwary, *ACS Appl. Mater. Interfaces*, 2025, **17**, 32973–32983.
43 S. Paul, S. Mishra, A. M B, P. Ghosh, P. Barman, M. Altvater, V. Pandey, P. P. Chanda, S. Das, A. Roy, N. R. Glavin, A. K. Singh and V. Kochat, *Small*, 2025, **21**, 2411297.
44 R. D. Salian, S. Mishra, C. C. Gowda, R. K. Barik, A. K. Singh, C. S. Tiwary and P. Kumbhakar, *Small Methods*, 2025, **9**(8), 2500068.
45 W.-H. Xie, W.-Y. Shiu and D. Mackay, *Mar. Environ. Res.*, 1997, **44**, 429–444.